ACS APPLIED MATERIALS & INTERFACES

www.acsami.org

Research Article

Influence of Microstructure on Mechanical and Electrical Properties of Indium Tin Oxide Thin Films Deposited on Polymer Substrates

Thibault Chommaux, Pierre-Olivier Renault,* Pierre Godard, and Dominique Thiaudière

Cite This: ACS Appl. Mater. Interfaces 2026, 18, 23364−23375

Read Online

ACCESS | Metrics & More | Article Recommendations

Downloaded via INIST-CNRS on June 5, 2026 at 11:37:14 (UTC).
See https://pubs.acs.org/sharingguidelines for options on how to legitimately share published articles.

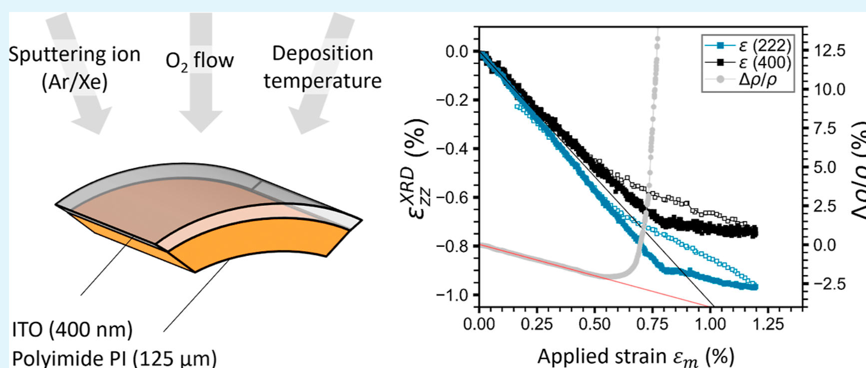

ABSTRACT: The electrical and mechanical behaviors of 400 nm thick indium tin oxide (ITO) thin films on polyimide substrates were investigated by means of electrical resistivity and synchrotron X-ray diffraction (XRD) measurements during equibiaxial tensile tests. Different microstructures were obtained with a change of the sputtering gas (argon or xenon), the deposition temperature (RT or 100 °C), or the oxygen partial pressure. The prepared ITO films are adhesive, crystalline even at room temperature deposition, and exhibit an electrical resistivity between 0.5×10^{-3} and 1.5×10^{-3} Ω·cm. It was observed that the use of argon during deposition leads to increased compressive residual stresses, resulting from the "atomic peening" effect, which induces point defect formation within the film. Results from deformation experiments highlight a dependence of ITO's elastic anisotropy on deposition conditions, closely associated with the preferential growth orientation of the film. The use of the Van der Pauw method during tensile loading allows for accurate identification of its piezoresistive response, characterized by a slightly negative gauge factor (−5.1 to −2.9). The mechanical and electrical integrity of ITO thin films, essential for their integration in flexible and transparent electronics, was assessed through the determination of the apparent and the intrinsic crack onset strain (COS), the latter accounting for the contribution of residual stresses. We show that compressive residual stresses enhance mechanical strength, but when they originate from point defects, as in this study, their beneficial effect is limited, thereby compromising the electrical and mechanical integrity of the films.

KEYWORDS: *ITO thin films, X-ray diffraction, tensile stress, piezoresistivity, mechanical anisotropy, crack initiation, mechanical properties, electrical properties*

INTRODUCTION

Indium tin oxide (ITO) is widely employed as transparent conductive electrodes in information and energy-related technologies due to its unique combination of high electrical conductivity and optical transparency in the visible spectrum. This dual functionality has led to its widespread adoption in optoelectronic devices such as liquid crystal displays (LCDs), organic light-emitting diodes (OLEDs), touch sensors, or solar cells.[1−6] As a result of the recent growth in stretchable microelectronics, the study of thin films on compliant substrates is receiving increased attention due to their promising applications, such as flexible displays or biosensors like sensory skins.[7−9] As with all oxide ceramics, the brittle nature of ITO poses limitations for devices that require flexibility, as it is prone to crack formation under mechanical stress. Nevertheless, ITO remains the most prevalent transparent electrode material.[10] Consequently, novel methodologies aimed at enhancing flexibility are under investigation, concentrating on alternative ITO morphologies, deposition techniques, or doping strategies.[11−13]

Received: October 29, 2025
Revised: April 8, 2026
Accepted: April 8, 2026
Published: April 14, 2026

ACS Publications © 2026 American Chemical Society

It is therefore essential to characterize and understand the intrinsic mechanical properties of indium tin oxide (ITO), as these properties play a critical role in determining the performance, reliability, and long-term stability of devices incorporating this material. Several studies have investigated the piezoresistivity of ITO,[14−16] the mechanical and electrical integrity of uniaxially deformed ITO thin films,[8,17−21] or the elastic anisotropy of ITO films.[22,23] However, the variability of results documented in the literature depends on the ITO microstructure, which itself is significantly influenced by the sputtering techniques employed. Various techniques have been reported for the deposition of ITO thin films, most of which rely on physical vapor deposition (PVD) methods such as electron-beam evaporation,[24] magnetron sputtering,[25] or pulsed laser deposition.[26] Thanks to its high degree of control over ion energy, flux and species combined with the ability to operate at low pressure, ion beam sputtering (IBS) appears as an attractive technique for low temperature deposition of ITO films.[27,28] However, despite the wide variety of deposition techniques reported in the literature, the relationship between deposition parameters, resulting microstructure, and functional properties is not always explicitly addressed or systematically established. It is therefore necessary to combine microstructural analysis with complementary characterization techniques in order to gain a deeper understanding of the underlying mechanisms governing the electro-mechanical behavior of these materials.

This article discusses the influence of microstructure on the electro-mechanical behavior of ITO thin films undergoing biaxial deformation. Previous studies conducted on ITO have already highlighted the relevance of integrating microstructure characterization into biaxial tensile testing.[29,30] In this work, several elaboration conditions (sputtering ion, oxygen partial pressure, and deposition temperature), which are intricately related to the presence of point defects,[27] were chosen to modify and control the microstructure of the samples. In situ monitoring of electrical and mechanical properties has been carried out thanks to the development of an experimental setup on the DiffAbs beamline at Synchrotron SOLEIL. This unique setup enables the investigation of critical parameters such as the crack onset strain, piezoresistivity, and elastic anisotropy of the films. Through this methodology, we identify and correlate the underlying mechanisms with the ITO microstructure, providing new insights into the electro-mechanical behavior of these materials.

■ METHODS

Ion Beam Sputtering Deposition

ITO thin films were deposited on 125-μm-thick polyimide (Kapton) substrates by ion beam sputtering (IBS) in a Nordiko 3000 chamber. Depending on the deposition conditions, argon or xenon ions were used as the primary source to sputter a sintered ceramic target composed of 90 wt % In_2O_3 and 10 wt % SnO_2. During deposition, the working pressure was around 1×10^{-4} and 3×10^{-4} mbar, respectively, for argon and xenon deposition. The ITO target is presputtered in three steps of 10 min in order to slowly increase its temperature and avoid any contamination. 400 nm-thick film deposits are performed with a growth rate of 0.14 nm·s^{-1} with Ar^+ and 0.20 nm·s^{-1} for Xe^+ ion beam (thickness samples were calibrated by ex situ X-ray reflectometry). In addition to the sputtering ion, O_2 reactive gas flow and substrate temperature are two optional conditions used to vary sample microstructure. A 5-sccm O_2 atmosphere is inserted without acceleration voltage through a second ion gun, and the temperature on the sample surface is set at 100 °C. A total of 6 depositions were carried out under varying conditions, as listed in Table 1, in order to obtain 6 different microstructures. Square thin films with dimensions of 12 × 12 mm^2 were deposited in the middle of the 200 mm and 20 mm wide cruciform polyimide (PI) substrates. The square shape of the film was chosen for the better reliability of the electrical measurements due to a reduction of the inaccuracies related to the positioning of the probes in the Van der Pauw geometry.[31]

Table 1. Elaboration Conditions for ITO Thin Films Deposited by Ion Beam Sputtering

sample set	sputtering ion (flow (sccm))	O_2 flow (sccm)	deposition temp. (°C)
Xe-RT	Xe (5)	×	RT
Xe+O_2-RT	Xe (5)	(5)	RT
Ar-RT	Ar (10)	×	RT
Ar+O_2-RT	Ar (10)	(5)	RT
Ar-100°C	Ar (10)	×	100
Ar+O_2-100°C	Ar (10)	(5)	100

XRD

ITO microstructure and internal stress were investigated by synchrotron X-ray diffraction. The synchrotron radiation allows the fine characterization of the mechanical behavior of films with extremely small diffracting volumes during a continuous tensile test. A double-crystal monochromator was used to monochromatize the incident X-ray beam to an energy of 18.00 keV (λ = 0.06888 nm). The size of the X-ray beam was approximately 280 × 240 μm^2 (horizontal and vertical FWHM, respectively). A hybrid pixel area detector (XPAD 2D detector), which covers a 2θ angular range of 6.75° with an incident ω angle of 7°, is used for the measurements. This facilitates the continuous tracking of the diffraction peaks associated with the (222) and (400) planes of ITO during tensile testing.

Tensile Test with In Situ Resistivity and Digital Image Correlation Measurements

This study aims to investigate the electrical and mechanical response of ITO thin films when undergoing a mechanical stress. To this end, we have integrated 4-point probe electrical measurements to the biaxial traction machine (locally developed[32,33]) situated at DiffAbs beamline of the French SOLEIL synchrotron facility as depicted in Figure 1. The arms of the cruciform-shaped substrate are gripped by four independent cylindrical motors, whose displacement was controlled to apply strain in the two perpendicular directions x and y of the polyimide substrate. The strain is then transferred to the ITO thin film in a homogeneous area in the middle of the substrate.

The backside of the substrates was spray-painted with a speckle pattern in order to determine the two in-plane macroscopic strains ε_{XX}^{DIC} and ε_{YY}^{DIC} using the digital image correlation (DIC) technique. For this purpose, 6 × 9 mm^2 images were taken at the center of the substrate for strain calculation.

The resistivity measurements were performed using the Van der Pauw technique. The latter, developed by Van der Pauw,[34] gives access to the sheet resistance $R_\square$ of a thin film with arbitrary shape by means of 8 four-point probe resistance measurements. These 8 measurements are conducted to eliminate potential electrometer shifts and resistance variations due to thermoelectric effects. Furthermore, this approach allows the resistance of the wire to be neglected, since no current is applied in the wires used for measuring the potential difference. The electrical resistivity is calculated from the sheet resistance $R_\square$ and film thickness d using the following eq 1

$$\rho = R_\square \times d \quad (1)$$

Note that electrical resistivity measurements are independent of its in-plane dimensions, which is particularly relevant in the case of in situ monitoring during a tensile test. The Van der Pauw technique has

https://doi.org/10.1021/acsami.5c21501
ACS Appl. Mater. Interfaces 2026, 18, 23364−23375

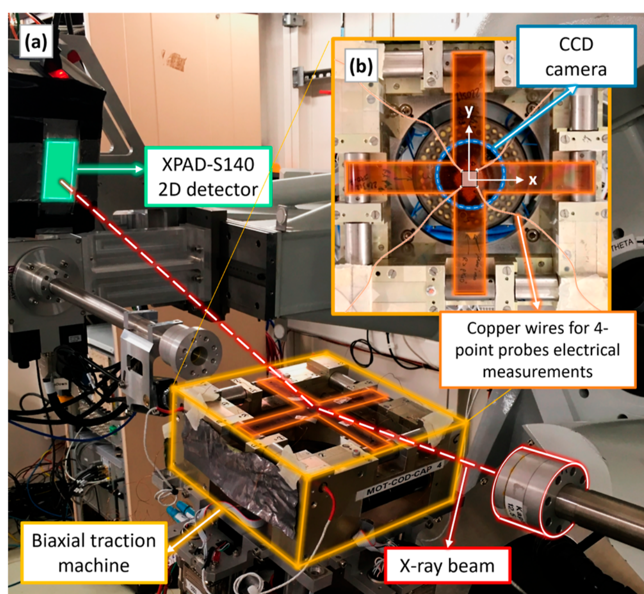

Figure 1. General view of the biaxial tensile tester installed on the Synchrotron SOLEIL DiffAbs beamline (a) and top close-up view of the tensile tester (b).

been implemented on the DiffAbs-SOLEIL biaxial tensile tester by running four copper wires to each corner of the square-shaped ITO films (see Figure 1b). The electrical contact between the wires and the sample was established through the application of silver paste.

The tensile machine (including DIC and Van der Pauw setup measurements) is mounted on a six-circle goniometer with a sample-to-detector distance of 717 mm. The equibiaxial tensile tests were carried out continuously by applying an identical displacement speed for each of the four motors of the tensile machine for each sample. Loading and unloading were conducted at a constant strain rate of 3.6 × 10^{-6} s^{-1}. XPAD diffractograms were recorded every 4 s during continuous biaxial loading and unloading, images for DIC analyses were also captured every 4 s, and resistivity was measured every 3 s.

RESULTS AND DISCUSSION

Initial State of Microstructural and Electrical Properties

The microstructural and electrical properties of ITO thin films were first characterized as-deposited in order to understand the influence of the deposition ion gas, O_2 flow, and substrate temperature on thin film growth, but also to determine the initial physical properties of our films elaborated by the IBS technique.

Though the role of the substrate is out of the scope of the present paper, we observed that grain orientation distributions and electrical resistivities are similar in ITO films deposited at RT on Kapton and on Si with a SiO_2 layer at the surface. It has also been shown that ITO films deposited on polyethylene terephthalate (PET) or on polyethylene naphthalate have similar mechanical and electrical behaviors.[35] It would be interesting to complement this study with other polymers, and in particular to compare PET with a polyimide. Note that the Kapton has a rather low thermal expansion coefficient (~20 × 10^{-6} °C^{-1}) as compared to the PET, and this will have an impact for films deposited at high temperature. Furthermore, ITO sputtered on Kapton is amorphous in the first tens of nanometers[29] and crystalline at later stages. The thickness associated with this transition may also depend on the substrate.

Synchrotron X-ray diffraction patterns of the as-deposited state of ITO thin films were reported in Figure 2. The

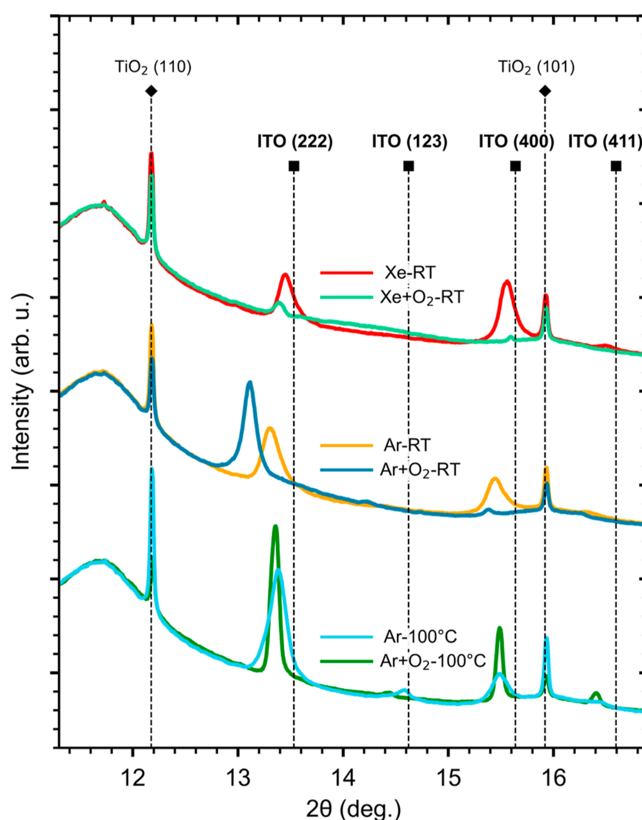

Figure 2. Typical X-ray diffractograms obtained for the initial state of the four deposition conditions from the XPAD detector with a collection time of 4 s. The TiO_2 powder is glued onto the substrate as a reference.

polyimide response is clearly identified as the large hump (with a peak around 2θ = 11.6°), which makes it difficult to distinguish between the crystalline and amorphous ITO phases. The (110) and (101) diffraction peaks related to TiO_2 powder used for DIC measurements allow XRD calibration and 2θ correction arising from vertical movement of the sample during loading tests. It should be noted that the amount of TiO_2 powder varies with the experiments; this explains the variation of its peak intensity but has no impact on the 2θ correction. With regard to the ITO microstructure, the diffraction peaks identified correspond to the bixbyite cubic structure of ITO reported in the ICDD database [PDF 04-014-4394]. The (222) and (400) diffraction peaks correspond to the two growth directions most frequently reported in the literature.[36,37] For each deposition condition, the angular position, full width at half-maximum (FWHM), and integrated area are the main features extracted from the diffraction patterns.

Crystallinity, Grain Size, and Crystallographic Texture

The presence of any crystallographic texture precludes a quantitative assessment of the crystallinity of the ITO films solely based on the integrated intensity of Bragg peaks. However, we notice that ITO films prepared with Xe + O_2-RT deposition conditions exhibit relatively low integrated intensity for the (222) and (400) Bragg peaks. Recorded diffractograms with a greater 2θ scale, from 11° to 33° (not reported here),

https://doi.org/10.1021/acsami.5c21501
ACS Appl. Mater. Interfaces 2026, 18, 23364−23375

present very low peak intensities for all the diffracting planes on this specific sample, confirming no texturing effect, thus an effective decrease of crystallinity for this sample. Moreover, the soft and large hump that can be seen between $2\theta = 13.5°$ and $2\theta = 15.5°$ was also observed by Legeay, who identified it as a signature of amorphous ITO.[38] In contrast, films deposited with argon as a sputtering ion exhibit a greater degree of crystallinity, even at room temperature. Lacroix et al. have found from SRIM calculations that backscattered Ar ions are more energetic (hundreds of eV) than Xe ions, inducing an "atomic peening" effect that can slightly increase the temperature of the substrate and thus enhance the crystallinity of the material.[27] This latter contribution can explain the low crystallinity of Xe + O_2-RT ITO thin film and the reason for obtaining well-crystalline ITO thin films deposited at room temperature by ion beam sputtering.

The grain size of the ITO microstructure is estimated from the FWHM and angular position of each diffraction peak using Scherrer's formula 2

$$D = K\frac{\lambda}{\beta_{\text{ech.}}\cos(\theta)} \quad (2)$$

With D the grain size, K a shape factor ($K = 0.9$[39]), λ the X-ray wavelength, θ the diffraction angle of the Bragg peaks, and $\beta_{\text{ech.}}$, the FWHM: $\beta_{\text{ech.}} = \sqrt{\beta^2_{\text{exp.}} - \beta^2_{\text{inst.}}}$, where β_{exp} . corresponds to the measured FWHM and $\beta_{\text{inst.}} = 0.03°$ corresponds to the instrumental resolution.

This relationship neglects the effects of microdistortion of the crystal lattice, which also widens the diffraction peak. The grain size values are therefore certainly underestimated, and the differences between samples may be caused by the annihilation of point defects. It should also be noted that for the diffraction conditions used here, the direction of measurement is normal to the surface of the sample. In the case of columnar growth, generally observed with textured materials, the measured value corresponds to the length of the columns. The average values of grain size D, obtained from the diffraction peaks (222) and (400), are reported in Table 2.

Table 2. Grain Size, Integrated Areas Ratio $A_{(222)}/A_{(400)}$ and Major Texture Component of Fiber Texture

sample set	grain size D (nm)	$A_{(222)}/A_{(400)}$	texture
Xe-RT	25	0.8	(100)
Xe+O_2-RT	38	8.9	(111)
Ar-RT	20	2.7	isotropic
Ar+O_2-RT	28	50	(111)
Ar-100°C	22	6.2	(111)
Ar+O_2-100°C	51	3.1	isotropic

These results should be considered with caution as they are likely to be underestimated, but they indicate that the grain size is nanometric and at least 20 nm, exceeding the electron mean free path in ITO (see Section Electrical Properties).

The crystallographic texture is one of the microstructural parameters that is useful to consider when characterizing mechanical behavior. Thus, surface roughness has been shown to be directly correlated with the growth direction of ITO films;[40] this subsequently alters their mechanical behavior.[41] Texture development during film growth is driven by thermodynamic forces aiming to reduce the total energy of the system. In particular, grains with orientations that minimize either the surface energy or the strain energy tend to grow preferentially.[42] Here, the proportion of grains with (222) and (400) planes parallel to the surface can be estimated from the diffraction patterns in Figure 2 using the ratio of the integrated areas of the (222) and (400) diffraction peaks: $A_{(222)}/A_{(400)}$. For an untextured film (or isotropically textured), this ratio is equal to 3.3 ([PDF 04-014-4394]); higher values indicate a (111) texture, while lower values suggest a (100) preferred orientation. The values of the $A_{(222)}/A_{(400)}$ ratio are reported in Table 2. For ITO thin films deposited at room temperature, Ar sputtering ions and O_2 flow promote a (111) texture, with an increased proportion of grains having (222) planes parallel to the surface. For films deposited at 100 °C, the insertion of O_2 flow does not follow the previous trend; it leads to a ratio close to 3.3, i.e., a non-textured system (isotropic texture).

Residual Stresses and Stress-Free Lattice Parameter

It is clearly visible that diffracting peaks of the ITO structure tend to shift toward small angles compared to the theory, as can be seen in Figure 2. These results can be put into perspective for the residual stress analysis. The mechanical state of ITO thin films at the initial state is investigated from measurements performed by the $\sin^2\Psi$ method. It is based on measuring the elastic strain $\varepsilon_{\Phi\Psi}$ along the direction defined by the angles Φ and Ψ. For a thin film subjected to in-plane isotropic stresses, the measured strain $\varepsilon_{\Phi\Psi}$ is related to the in-plane macroscopic residual stress σ_r by the following expression (eq 3)[43]

$$\varepsilon_{\Phi\Psi} = \frac{1}{2}S_2^{hkl}\sigma_r\sin^2\Psi + S_1^{hkl}2\sigma_r \quad (3)$$

With $\frac{1}{2}S_2^{hkl}$ and S_1^{hkl}, the hkl-dependent X-ray diffraction elastic constants (XEC). For cubic materials, one gets a linear dependence of both XECs versus the orientation parameter $\Gamma(hkl) = \frac{(h^2k^2 + h^2l^2 + k^2l^2)}{(h^2 + k^2 + l^2)^2}$. In addition, these two diffraction elastic constants can be expressed as functions of hkl-dependent Young's modulus E^{hkl} and Poisson's ratio ν^{hkl} (eq 4)

$$\frac{1}{2}S_2^{hkl} = \frac{1 + \nu^{hkl}}{E^{hkl}}$$
$$S_1^{hkl} = \frac{-\nu^{hkl}}{E^{hkl}} \quad (4)$$

The average of $\frac{1}{2}S_2^{hkl}$ taken over all lattice directions hkl is connected to the macroscopic constants Young's modulus E and Poisson's ratio ν and, is obtained for $\Gamma = 0.2$: $\frac{1}{2}S_2^{\text{mech.}} = (1 + \nu)/E = \frac{1}{2}S_2$ ($\Gamma = 0.2$). Then, the logarithm of the lattice parameter $\ln(a)$ can be written as a function of $\sin^2\Psi$ as follows (eq 5)

$$\ln(a) = \frac{1}{2}S_2^{hkl}\sigma_r\sin^2\Psi + S_1^{hkl}2\sigma_r + \ln(a_0) \quad (5)$$

The acquisition of diffraction images collected at $\Phi = 0°$ and Ψ varying from 0° to 70° in 5° steps made it possible to plot the logarithm of the lattice parameter $\ln(a)$ as a function of $\sin^2\Psi$. Figure 3 shows the $\ln(a) - \sin^2\Psi$ curves for the (222) and (400) planes for each deposition condition. Observe that the two planes, (hhh) and (h00), exhibit the highest and lowest stiffness, respectively, according to the Zener anisotropy factor.

https://doi.org/10.1021/acsami.5c21501
ACS Appl. Mater. Interfaces 2026, 18, 23364−23375

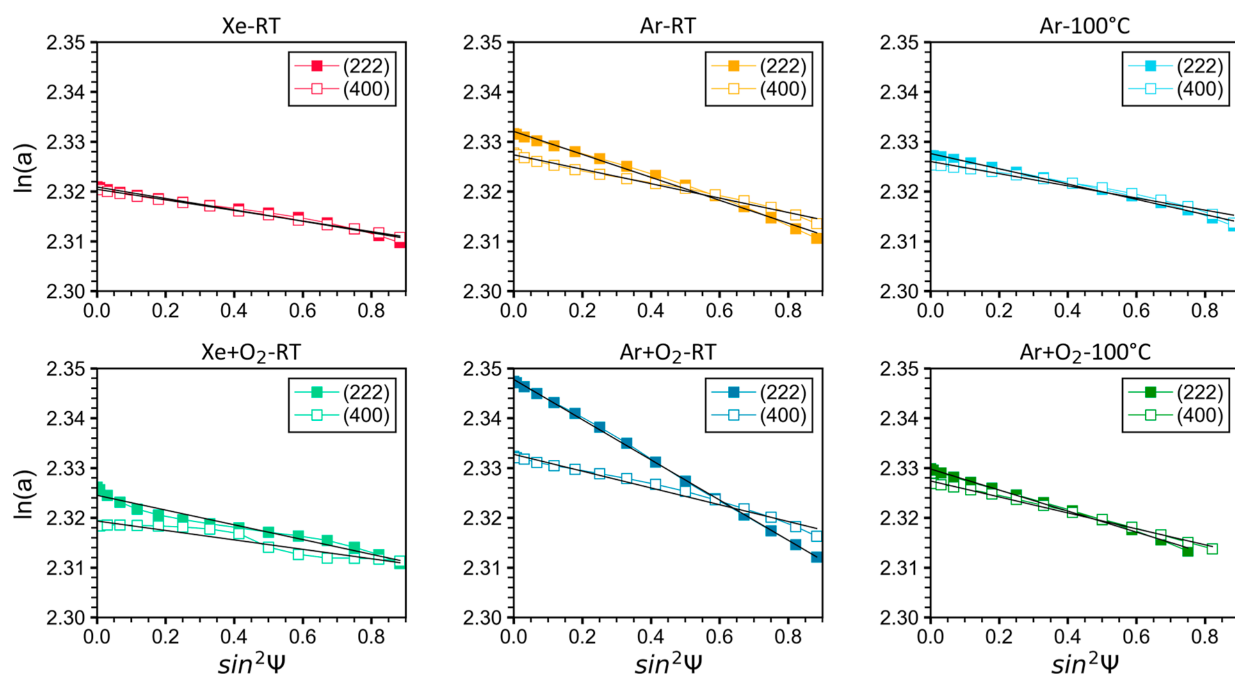

Figure 3. Evolution of the logarithm of the lattice parameter ln(a) as a function of $\sin^2 \Psi$ for the (222) and (400) planes for each ITO thin film deposition condition.

For all six samples, a quasi-linear evolution is observed. First, the negative slopes of ln(a) versus $\sin^2 \Psi$ indicate an as-deposited compressive stress state for all ITO films. Second, the results show that the slopes characteristic of (222) planes and (400) planes are nearly identical for three samples, which reflects that the films have a Zener anisotropy factor close to 1. The difference between the two slopes is becoming more apparent for two samples, namely Ar-RT and Xe + O_2-RT, and Ar + O_2-RT exhibits significant different slopes $\left(\frac{1}{2}S_2^{400}/\frac{1}{2}S_2^{222} = 0.4\right)$, highlighting elastic anisotropy with a Zener anisotropy factor much smaller than 1. By combining the frequency signatures of the vibrational modes of ITO nanorods with finite-element simulations, Guo et al. determined the three elastic stiffnesses for crystalline cubic ITO: c_{11} = 277.5 GPa, c_{12} = 107 GPa, and c_{44} = 33.8 GPa.[22] These stiffness values lead to a strong elastic anisotropy with a Zener anisotropy index of 0.39. This value corroborates qualitatively the fact that the [400] direction is stiffer than the [222] direction as also observed by Veith et al.[23] Thus, the X-ray elastic constants (XEC), $\frac{1}{2}S_2^{222}$ = 11.99 × 10^{-6} MPa^{-1} and $\frac{1}{2}S_2^{400}$ = 7.53 × 10^{-6} MPa^{-1}, can be calculated from the stiffnesses c_{ij} using the Neerfeld−Hill model (average of Reuss and Voigt models[43]). However, as our results show that elastic anisotropy varies from one sample to another, we propose to calculate the stresses based on three different assumptions that provide a better understanding of the influence of the models. First, we have used the X-ray Elastic Constants (XEC) calculated from Guo's stiffnesses $\frac{1}{2}S_2^{222}$ = 11.99 × 10^{-6} MPa^{-1} and $\frac{1}{2}S_2^{400}$ = 7.53 × 10^{-6} MPa^{-1}. From these XECs, we calculated the stress values for the six samples (thus neglecting changes in anisotropy from one sample to another). Second, we can calculate the stresses in a very simplistic way using the macroscopic elasticity constants: $\frac{1}{2}S_2^{\text{mech.}}$ = (1 + 0.35)/132 = 10.23 × 10^{-6} MPa^{-1}. The Young's modulus value of 132 GPa was chosen to maintain the same elastic modulus as that calculated from Guo's stiffness values.[22] Noteworthy, this represents a 14% deviation from a modulus of 116 GPa that has been used in the work of Veith et al.[23] Obviously, with this assumption, as we have two slopes with a single coefficient, we obtain two stress values. To get only one, we weight according to the deviation from the mechanical value: $\sigma = \sigma^{222}_{\text{measured}} \times (0.2{-}0) + \sigma^{400}_{\text{measured}} \times (0.333{-}0.2)$ keeping in mind that $\Gamma(400) = 0$ and $\Gamma(222) = 0.333$. Third, we can exploit our data to the maximum to estimate the XECs by using the ratio of the XECs measured directly with the slopes, on the one hand, and by maintaining the Young's modulus of the material at the value of 132 GPa estimated from Guo's c_{ij} values, on the other. In other words, in this third assumption, we maintain $\frac{1}{2}S_2^{\text{mech.}}$ = $\frac{1}{2}S_2$ (Γ = 0.2) = 10.23 × 10^{-6} MPa^{-1} to estimate the values $\frac{1}{2}S_2^{400}$ and $\frac{1}{2}S_2^{222}$. This is based on the fact that, in the case of cubic materials, $\frac{1}{2}S_2^{hkl}$ is a linear function of the factor $\Gamma(hkl)$. Figure 4 presents a comparison of the stress values obtained using the three different assumptions. For each sample, the results are in good agreement, with a maximum deviation of 4%. This indicates that the choice of stress evaluation method has a limited impact compared to the differences observed between samples.

To quantify the elastic anisotropy of the films based on the $\sin^2 \Psi$ measurements, the Zener anisotropy factor is calculated using the compliance coefficients derived from the third assumption. The values obtained are summarized in the Table 3.

The stress-free lattice parameter can be determined in a similar way to the stress, using eq 5 and the intercepts of each curve shown in Figure 3. The values were calculated based on the third assumption (previously used for the stress calculations), i.e., by calculating the XECs from the results of this work. The stress-free lattice parameters are summarized in

https://doi.org/10.1021/acsami.5c21501
ACS Appl. Mater. Interfaces 2026, 18, 23364−23375

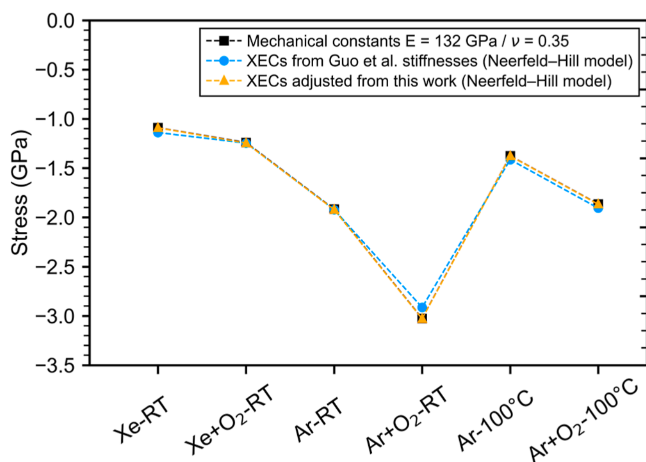

Figure 4. Stress evolution for each ITO thin film and the three proposed assumptions.

Table 3. Zener Anisotropy Factor A_{Zener}

sample set	A_{Zener}
Xe-RT	0.85
Xe+O_2-RT	0.41
Ar-RT	0.40
Ar+O_2-RT	0.20
Ar-100°C	0.65
Ar+O_2-100°C	0.58

Figure 5. These are all greater than or equal to a_0 = 10.126 Å, i.e., the ITO reference lattice parameter ([PDF 04-014-4394]).

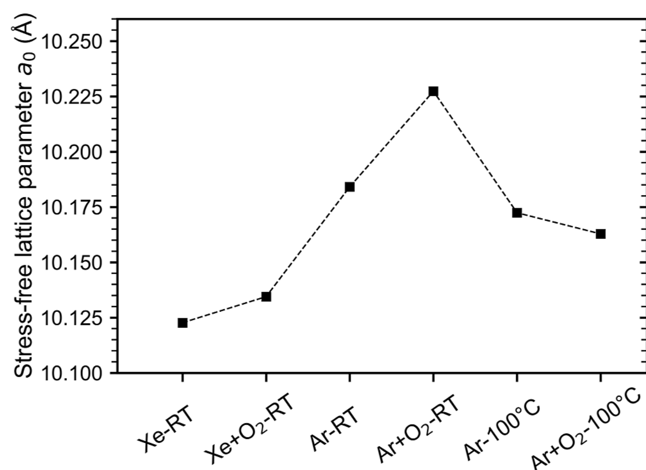

Figure 5. Summary of stress-free lattice parameter a_0 for each ITO thin film deposition condition.

Above this value, it suggests the presence of point defects in the microstructure. In fact, stress-free lattice parameter is often used to assess for point defects.[44−47] A marked increase in a_0 is observed in the case of thin films deposited with Ar ions. This can be explained by the "atomic peening" effect, as mentioned previously, which can lead to the creation of defects such as anti-Frenkel pairs, oxygen vacancies, oxygen interstitial, or backscattered Ar ion incorporation.[48] Moreover, it is noteworthy that applying an O_2 partial pressure during room temperature deposition also leads to a significant increase in a_0.

Electrical Properties

The as-deposited electrical characteristics were characterized by Hall effect measurements in an HMS 5500 setup. Resistivity ρ and charge carrier concentration n were determined using the Van der Pauw method, with a field strength B = 0.58 T. Hall mobility μ is then calculated using the following equation: $1/\rho = qn\mu$. The results of the six samples are compared in Figure 6.

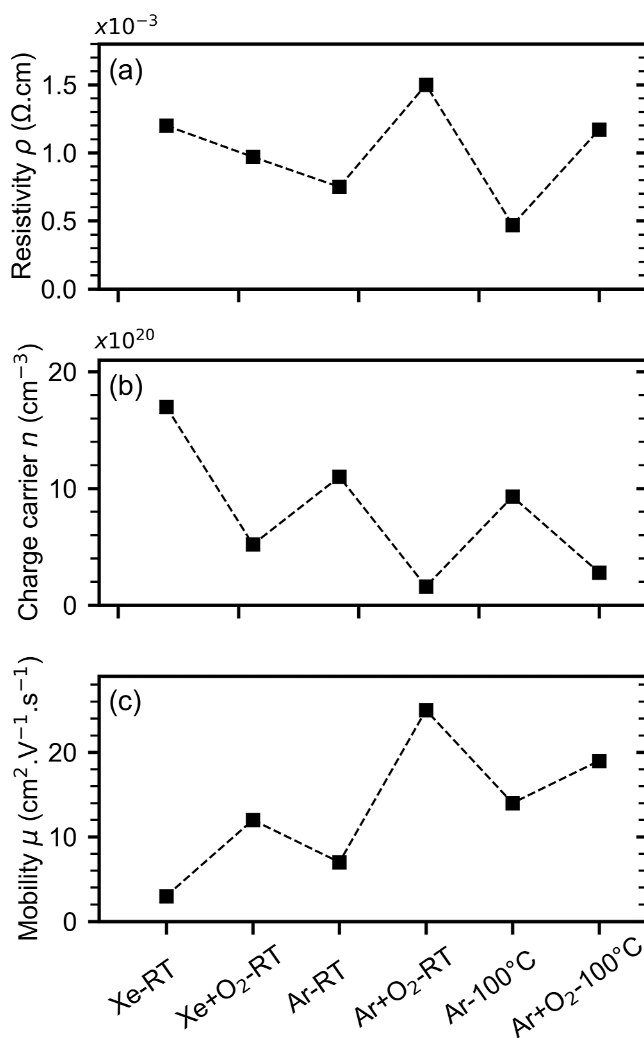

Figure 6. Summary of electrical resistivity (a), charge carrier concentration (b), and charge carrier mobility (c) for each ITO thin film deposition condition.

Analysis of the electrical resistivity data (Figure 6a) reveals that the most resistive sample is the one deposited with Ar + O_2-RT conditions, while the least resistive corresponds to the one deposited with Ar-100 °C conditions. The latter result can be interpreted in terms of the number of charge carriers and their mobility (Figure 6b,c).

First, it should be noted that the measured carrier concentrations are negative; by convention, this means that the majority charge carriers are electrons. However, the values in Figure 6 are presented as absolute values. Overall, ITO samples have a charge carrier density above $n_c \approx 10^{19}$ cm^{-3} which corresponds to the critical threshold above which a material is typically classified as a degenerate semiconductor according to Edwards and Sienko.[49] The ITO thin films

https://doi.org/10.1021/acsami.5c21501
ACS Appl. Mater. Interfaces 2026, 18, 23364−23375

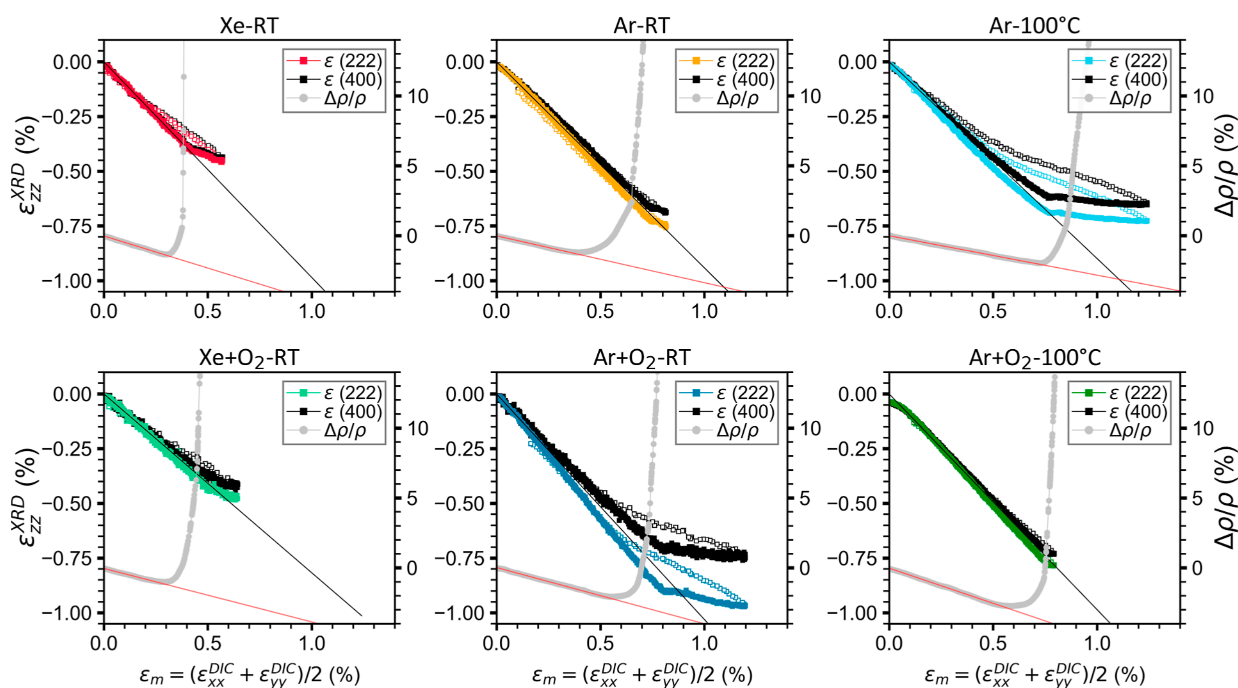

Figure 7. (222) and (400) ITO strains $\varepsilon(222)$ and $\varepsilon(400)$ and relative change in resistivity $\Delta\rho/\rho_0$ as functions of the applied strain ε_m for the six ITO thin films during tensile test. Strain values are represented in full (respectively open) symbols for the loading (respectively unloading). For a better visualization, the $\Delta\rho/\rho_0$ values are only plotted for the beginning of the tensile test.

studied here are therefore considered to be n-type degenerate semiconductors.

With regard to the influence of deposition parameters, it is noteworthy that the prevailing effect on the electron concentration is the presence or absence of O_2 flow during deposition. With the addition of 5 sccm of O_2 during deposition, the number of charge carriers is significantly reduced. This decrease can be explained as follows: constitutionally, the bixbyite-type structure of ITO exhibits an oxygen vacancy concentration of 25%. These vacancies act as double charge carrier donor sites.[50] When a partial pressure of oxygen is introduced during deposition, this causes the annihilation of some of the intrinsically present oxygen vacancies. This consequently leads to a reduction in the charge carrier density. Concerning the impact of the ion, the crystallinity is sometimes referred to in the literature as a factor that increases the number of charge carriers in the material.[27,51] In the present case, crystallinity does not play a major role in the value of n, as Xe-ion-deposited thin films exhibit the highest charge carrier concentrations (for the same O_2 flow condition). These results further refine the previously reported conclusion regarding point defects. Specifically, they enable the correlation between the increase in the stress-free lattice parameter of ITO films deposited using Ar ions and a 5 sccm O_2 flow and a decrease in the number of oxygen vacancies.

The evolution of electrical mobility with varying deposition conditions indicates that both the Ar ion and the addition of O_2 flow contribute to its enhancement. This suggests that the main obstacle to mobility is the diffusion of electrons by ionized or neutral impurities. One way to confirm this is to calculate the mean free path l, defined below (eq 6) using a degenerate electron gas model[52]

$$l = (3\pi^2)^{1/3}(he^{-2})\rho^{-1}n^{-2/3} \quad (6)$$

With h the Planck's constant, e the electron charge. Therefore, grain boundaries have an influence on electrical mobility if the size of the grain is comparable to the mean free path l of electrons. In our case, the calculated values of l are between 5 and 18 nm, which is lower than the grain sizes reported in the previous section from diffraction patterns. This means that the intragrain scattering by ionized or neutral impurities is dominating the grain boundary scattering.[52] The doubly charged oxygen vacancies or singly charged tin seem to be the major obstacle for electrical conduction in ITO films. This is further supported by the low crystallinity of the Xe + O_2-RT film not affecting the electrical mobility.

In Situ Tensile Test: Mechanical and Electrical Behavior

The main objective of this study is to investigate the electromechanical behavior of different ITO films in order to understand the influence of microstructure on electrical and mechanical properties during mechanical loading and unloading. Experimentally, elastic out-of-plane strain ε_{ZZ}^{XRD}, in-plane macroscopic strains ε_{XX}^{DIC} and ε_{YY}^{DIC} and resistivity ρ are respectively obtained from XRD measurements, digital image correlation measurements, and electrical resistivity measurements using the Van der Pauw method. We assume that there is full transmission of the strain from the substrate to the film, i.e., without any loss of adhesion of the thin film. This assumption is confirmed, first qualitatively using the tape method,[53,54] and second quantitatively by tests carried out in step-by-step mode, with strain measurements in several directions Ψ for a given mechanical state[33] or in continuous mode.[55,56] Finally, in ref 29, we showed that the strain transmission was complete through the different layers of an ITO/Ag/ITO stacking deposited on Kapton. The reason for this adhesion lies in the energetic deposition process.[57,58]

The (222) and (400) ITO strains $\varepsilon(222)$ and $\varepsilon(400)$ and the relative change in resistivity are respectively plotted versus the applied macroscopic strain $\varepsilon_m = (\varepsilon_{XX}^{DIC} + \varepsilon_{YY}^{DIC})/2$ in Figure

https://doi.org/10.1021/acsami.5c21501
ACS Appl. Mater. Interfaces 2026, 18, 23364−23375

7. The black line represents the macroscopic strain (corresponding to a quasi-isotropic polycrystal). The red line is extrapolated from the linear regime of $\Delta\rho/\rho_0$ values. Note that the maximum macroscopic strain (corresponding to the strain at which the mechanical loading is ended) differs from one experiment to another. This is related to the criterion for stopping the mechanical loading, which is based on the measurement of electrical resistivity and not on the XRD measurement.

For each sample, 4 domains are identified for strain values during the tensile test. The first linear evolution of $\varepsilon(222)$ and $\varepsilon(400)$ is characteristic of the elastic regime of ITO films. The beginning of the second domain is characterized by an abrupt change in the slope, which is attributed to the nucleation of cracks within the film. When a crack forms, it induces stress relaxation around its vicinity, leading to a reduction in the average stress in the film. Consequently, the change in the slope of the elastic strain versus applied strain curve can statistically be considered as an indicator of the presence of cracks within the material. During mechanical unloading, a third domain reflects a crack closure process that is slower than the cracking process, resulting in the opening of a hysteresis loop. The fourth domain is overlapped with domain 1, which is characteristic of an elastic recovery of the material.

Regarding the relative change in electrical resistivity, two domains are identified during mechanical loading: a first domain where the evolution is linear and slightly decreasing, followed by a domain where $\Delta\rho/\rho_0$ increases strongly, indicating a major disturbance of the conduction channels, characteristic of the cracking process in ITO film.

Elastic Anisotropy

The comparison between the lattice strains $\varepsilon(222)$ and $\varepsilon(400)$ during the elastic regime is directly related to the elastic anisotropy of the thin films. Here again, the ratio of the slopes $\varepsilon(400)/\varepsilon(222)$ in the elastic regime demonstrates that the ITO thin films exhibit elastic anisotropy, with the [400] direction stiffer than the [222] direction. Notably, the same trend is observed in both experimental approaches: (i) from the measurement of as deposited stress state on both (222) and (400) diffraction peaks, and (ii) from the in situ mechanical test and measurements on both (222) and (400) diffraction peaks. The observed variations in elastic anisotropy can be correlated with their microstructure. In polycrystalline materials, the macroscopic anisotropy of the layer may be related to the non-random orientation of the grains.[23,59] Here, the sample with the highest elastic anisotropy corresponds to the one with a strong grain orientation along the direction [111] perpendicular to the surface. More generally, for the six sample series, it is verified that the greater the $A_{(222)}/A_{(400)}$ ratio (see Table 2), the greater the elastic anisotropy.

ITO Piezoresistivity

The relative changes in electrical resistivity $\Delta\rho/\rho_0$ of each sample are plotted versus the applied macroscopic strain on a common graph in Figure 8. For a better visualization of the experimental data, only the beginning of the tensile test is presented. Note that the resistivity values were smoothed using the LOWESS function (frac = 0.125).[60] Here, the ratio $\Delta\rho/\rho_0$ corresponds to the ratio $\Delta R_{\square}/R_{\square}$, obtained by solving Van der Pauw's equation (see eq 1), which takes into account the variation in film thickness $\Delta d/d$, i.e., the out-of-plane elastic strain $\varepsilon_{ZZ}^{\mathrm{XRD}}$.

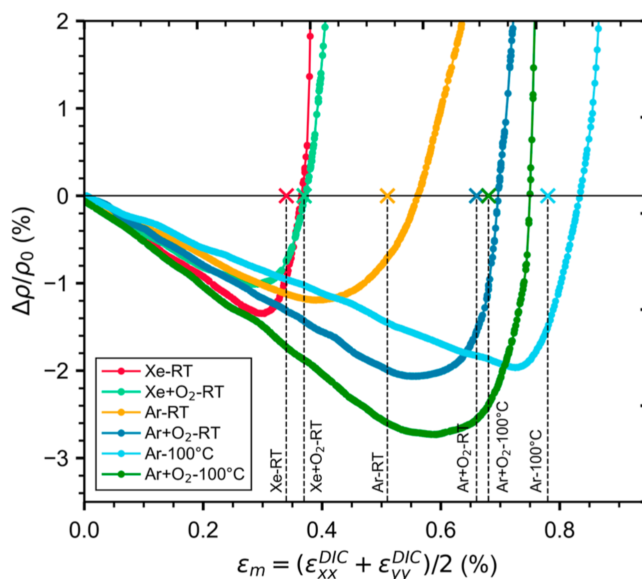

Figure 8. Relative changes in electrical resistivity at the beginning of the tensile tests.

In the elastic regime, the linear and decreasing $\Delta\rho/\rho_0$ behavior is characteristic of a piezoresistive response of the ITO. An intrinsic gauge factor $G_{\mathrm{intr.}}$ is subsequently introduced in order to quantify the relative changes in electrical resistivity as a function of applied macroscopic strain, independently of geometrical effects (eq 7). This parameter benefits from the high temporal resolution and measurement accuracy offered by the in situ 4-point probes Van der Pauw setup, enabling the detection of subtle strain-induced effects.

$$G_{\mathrm{intr.}} = \frac{\Delta\rho/\rho_0}{\varepsilon_{\mathrm{macro}}} = \frac{\Delta\rho/\rho_0}{(\varepsilon_{XX}^{\mathrm{DIC}} + \varepsilon_{YY}^{\mathrm{DIC}})/2} \quad (7)$$

The gauge factors determined for each sample are given in Table 4. The values are systematically negative and range from −5.1 to −2.9. The negative value of $G_{\mathrm{intr.}}$ indicates that in the elastic regime, the electrical resistivity of ITO thin films decreases as the film is subjected to increasing deformation, contrary to metallic materials. In the work conducted by Fang et al.,[14] the negative gauge factor is attributed to a hopping conduction mechanism in oxygen-rich amorphous ITO films. The authors suggest that increasing the oxygen content enhances structural disorder, leading to a higher density of localized states near the mobility edge. As the oxygen concentration rises, they propose a transition in the conduction mechanism from extended-state transport at low oxygen content to thermally activated hopping conduction in films with higher oxygen content. Following this reasoning, the negative gauge factor values are expected to depend on two

Table 4. Intrinsic Gauge Factor $G_{\mathrm{intr.}}$

sample set	gauge factor $G_{\mathrm{intr.}}$ ± 0.1
Xe-RT	−4.7
Xe+O_2-RT	−3.8
Ar-RT	−3.5
Ar+O_2-RT	−3.9
Ar-100°C	−2.9
Ar+O_2-100°C	−5.1

https://doi.org/10.1021/acsami.5c21501
ACS Appl. Mater. Interfaces 2026, 18, 23364−23375

main parameters: the oxygen content, which is indirectly assessed through the carrier density, and the fraction of the amorphous phase within the film. Since the latter parameter was not quantified in the present study, we can only hypothesize that these two factors contribute to the piezoresistive behavior observed in our films. Furthermore, electrical mobility and charge carrier concentration could not be measured during the in situ tensile tests, which limits the discussion of the underlying physical mechanisms responsible for the negative gauge factor values. However, from an application perspective, the relatively small variations in the gauge factor indicate that this factor is robust with respect to these microstructural variations, which is a relevant and informative outcome.

Mechanical and Electrical Integrity

As explained previously, the loss of linearity of elastic strain as a function of the applied macroscopic strain ε_m is attributed to the end of the elastic regime. This abrupt transition is indicative of the brittle nature of ITO. Due to the high density of measurement points, the macroscopic strain ε_m at which cracking appears, the so-called crack onset strain (COS), can be quantified precisely. The COS is graphically measured at the intersection of domain 1 (elastic regime) and domain 2 (cracking regime). It is also possible to determine a crack onset strain from electrical resistivity measurements. The strong increase of $\Delta\rho/\rho_0$ is characteristic of thin film cracking. In our case, the COS values correspond to the macroscopic strain ε_m at which a 1% increase in $\Delta\rho/\rho_0$ is detected (as marked by the crosses in Figure 8). The choice of this low threshold is made possible by the high resolution of the electrical measurements. The COS values obtained from both XRD and $\Delta\rho/\rho_0$ measurements are plotted in Figure 9 for each sample. These are referred to as apparent COS. These results are compared with the macroscopic residual strain derived from stress values presented in Figure 4. An intrinsic COS is also reported, which corresponds to the sum of the XRD crack onset strain and the macroscopic residual strain, based on studies conducted by Leterrier et al.[19]

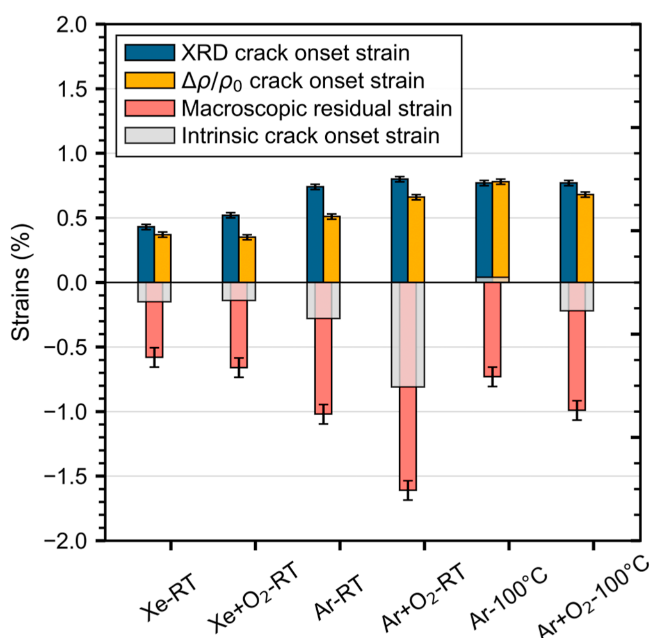

Figure 9. Summary of crack onset strain measured from XRD and electrical resistivity measurements, compared to the macroscopic residual strain. The calculated intrinsic crack onset strain equals the sum of the macroscopic residual strain and the XRD crack onset strain.

Comparing apparent XRD crack onset strain and $\Delta\rho/\rho_0$ crack onset strain shows that electrical measurements anticipate the detection of the cracking process, except for one sample (Ar-100 °C). This anticipated evaluation, as already observed in a previous study,[29] can be explained from a statistical point of view. The two methods do not probe the same quantity of material. XRD measurements probe a lateral zone of 0.25 × 3 mm^2, whereas the electrical measurements probe the entire film. Consequently, the first nucleated crack in the film will inevitably have an influence on the electrical measurement but will have no effect on the XRD measurement if it is not located under the X-ray beam. Overall, thin films deposited with argon ions exhibit a higher apparent COS. This result correlates with the parallel increase in the macroscopic residual strain. It has therefore been verified that compressive residual stresses are beneficial for the mechanical integrity of ITO thin films subjected to tensile loading, which is generally the case for adherent thin films.[61]

Discussing the intrinsic COS is particularly relevant as it provides information on the mechanical behavior of the ITO film alone, similarly to investigations carried out on free-standing materials.[62] Interestingly, we note that cracking occurs when the films are in a compression state (slightly in tension for the Ar-100 °C sample). Comparison between the different samples reveals a trend similar to that of the free-lattice parameter, which is directly related to the introduction of point defects resulting from the "atomic peening" effect. The presence of a higher density of defects could influence crack propagation and account for the more brittle behavior of ITO films deposited with Ar ions and O_2 flow. Thus, while compressive residual stresses appear to be beneficial for increasing the crack onset strain (COS), their origin plays a crucial role. If such stresses are associated with a high density of point defects, as seems to be the case for films deposited at room temperature, this may lead to a degradation of the film's mechanical integrity.

■ CONCLUSION

The electrical and mechanical behavior of crystalline indium tin oxide thin films subjected to equi-biaxial deformation was investigated in relation to their microstructure. This study was conducted using an in situ multiscale approach combining elastic strain measurements by synchrotron X-ray diffraction, macroscopic strain measurements by digital image correlation (DIC), and electrical resistivity measurements. The use of synchrotron radiation (DiffAbs beamline—SOLEIL synchrotron) allows for a detailed characterization of the mechanical response of films with low diffraction volume during continuous tensile loading and unloading.

The findings demonstrate that ITO exhibits variable elastic anisotropy depending on the deposition conditions, closely correlated with the preferential growth orientation of the film. This result was obtained using two independent methods: from $\sin^2\Psi$ measurements of the as-deposited stress state and from the in situ tensile tests. Based on first method, the Zener anisotropy factor was determined, ranging from A_{Zener} = 0.2 for the most anisotropic sample (Ar + O_2-RT) to A_{Zener} = 0.85 for the most isotropic sample (Xe-RT). Thanks to the implementation of the Van der Pauw method during the

https://doi.org/10.1021/acsami.5c21501
ACS Appl. Mater. Interfaces 2026, 18, 23364−23375

tensile test, the piezoresistive behavior of ITO is precisely revealed with a slightly negative gauge factor ranging from −5.1 to −2.9.

These experiments provide simultaneous access to the mechanical and electrical integrity of ITO thin films, two key properties for their use in flexible and transparent electronics. The results show that increasing residual compressive stresses leads to a higher apparent COS. However, by taking into account the contribution of residual stresses, it is possible to extract an intrinsic COS that reflects the true mechanical strength of the ITO itself. This intrinsic COS suggests that films with a higher density of point defects exhibit reduced fracture resistance. Although compressive residual stresses are beneficial for mechanical integrity, their origin, primarily from point defects in this study, limits their positive effect. This contradictory effect is revealed through the comparison between the apparent and intrinsic COS values. Therefore, identifying alternative ways to induce compressive residual stresses, without introducing defects, could be a promising strategy to enhance both mechanical and electrical performance.

AUTHOR INFORMATION

Corresponding Author

Pierre-Olivier Renault − *Department of Physics and Mechanics of Materials, Pprime Institute—CNRS, University of Poitiers, 86073 Poitiers, France*;
Email: pierre.olivier.renault@univ-poitiers.fr

Authors

Thibault Chommaux − *Department of Physics and Mechanics of Materials, Pprime Institute—CNRS, University of Poitiers, 86073 Poitiers, France; Synchrotron SOLEIL, 91190 Gif-sur-Yvette, France*; orcid.org/0000-0001-8456-728X

Pierre Godard − *Department of Physics and Mechanics of Materials, Pprime Institute—CNRS, University of Poitiers, 86073 Poitiers, France*

Dominique Thiaudière − *Synchrotron SOLEIL, 91190 Gif-sur-Yvette, France*

Complete contact information is available at:
https://pubs.acs.org/10.1021/acsami.5c21501

Notes

The authors declare no competing financial interest.

ACKNOWLEDGMENTS

The authors gratefully acknowledge SOLEIL for beam time allocation and C. Mocuta for help during the experiments. The authors thank Ph. Goudeau for general discussion. This work was partially funded by the French Government programs "Investissement d'Avenir" (LABEX INTERACTIFS, reference ANR-11-LABX-0017-01, EUR INTREE, reference ANR-18-EURE-0010). The region Nouvelle-Aquitaine and the French synchrotron SOLEIL via the NACRES project supported this work.

REFERENCES

(1) Gordon, R. G. Criteria for choosing transparent conductors. *MRS Bull.* **2000**, *25*, 52−57.

(2) Ensch, M.; Wehring, B.; Landis, G. D.; Garratt, E.; Becker, M. F.; Schuelke, T.; Rusinek, C. A. Indium tin oxide film characteristics for cathodic stripping voltammetry. *ACS Appl. Mater. Interfaces* **2019**, *11*, 16991−17000.

(3) Helander, M.; Wang, Z.; Qiu, J.; Greiner, M.; Puzzo, D.; Liu, Z.; Lu, Z. Chlorinated indium tin oxide electrodes with high work function for organic device compatibility. *Science* **2011**, *332*, 944−947.

(4) Macher, S.; Rumpel, M.; Schott, M.; Posset, U.; Giffin, G. A.; Lobmann, P. Avoiding voltage-induced degradation in PET-ITO-based flexible electrochromic devices. *ACS Appl. Mater. Interfaces* **2020**, *12*, 36695−36705.

(5) Yu, Z.; Perera, I. R.; Daeneke, T.; Makuta, S.; Tachibana, Y.; Jasieniak, J. J.; Mishra, A.; Bäuerle, P.; Spiccia, L.; Bach, U. Indium tin oxide as a semiconductor material in efficient p-type dye-sensitized solar cells. *NPG Asia Mater.* **2016**, *8*, No. e305.

(6) Ellmer, K. Past achievements and future challenges in the development of optically transparent electrodes. *Nat. Photonics* **2012**, *6*, 809−817.

(7) Rogers, J. A.; Someya, T.; Huang, Y. Materials and Mechanics for Stretchable Electronics. *Science* **2010**, *327*, 1603−1607.

(8) Cairns, D. R.; Witte, R. P.; Sparacin, D. K.; Sachsman, S. M.; Paine, D. C.; Crawford, G. P.; Newton, R. Strain-dependent electrical resistance of tin-doped indium oxide on polymer substrates. *Appl. Phys. Lett.* **2000**, *76*, 1425−1427.

(9) Park, S. K.; Han, J. I.; Moon, D. G.; Kim, W. K. Mechanical stability of externally deformed indium−tin−oxide films on polymer substrates. *Jpn. J. Appl. Phys., Part 1* **2003**, *42*, 623.

(10) Althumayri, M.; Das, R.; Banavath, R.; Beker, L.; Achim, A. M.; Ceylan Koydemir, H. Recent advances in transparent electrodes and their multimodal sensing applications. *Adv. Sci.* **2024**, *11*, 2405099.

(11) Dong, Q.; Hara, Y.; Vrouwenvelder, K. T.; Shin, K. T.; Compiano, J. A.; Saif, M.; Lopez, R. Superflexibility of ITO electrodes via submicron patterning. *ACS Appl. Mater. Interfaces* **2018**, *10*, 10339−10346.

(12) Datta, R. S.; Syed, N.; Zavabeti, A.; Jannat, A.; Mohiuddin, M.; Rokunuzzaman, M.; Yue Zhang, B.; Rahman, M.; Atkin, P.; Messalea, K. A.; et al. Flexible two-dimensional indium tin oxide fabricated using a liquid metal printing technique. *Nat. Electron.* **2020**, *3*, 51−58.

(13) Taha, H.; Jiang, Z.-T.; Henry, D. J.; Amri, A.; Yin, C.-Y.; Alias, A. B.; Zhao, X. Improved mechanical properties of sol-gel derived ITO thin films via Ag doping. *Mater. Today Commun.* **2018**, *14*, 210−224.

(14) Fang, H.; Miller, T.; Rogers, B.; Magruder, R., III; Weller, R. Effect of oxygen content on piezoresistivity of indium tin oxide thin films prepared by pulsed laser deposition. *J. Appl. Phys.* **2005**, *97*, 083502.

(15) Dyer, S.; Gregory, O.; Amons, P.; Slot, A. B. Preparation and piezoresistive properties of reactively sputtered indium tin oxide thin films. *Thin Solid Films* **1996**, *288*, 279−286.

(16) Yang, S.; Zhang, C.; Chang, X.; Huang, J.; Yang, Z.; Yao, J.; Wang, H.; Ding, G. Effect of heat treatment atmosphere on the piezoresistivity of indium tin oxide ceramic strain sensor. *Ceram. Int.* **2019**, *45*, 17048−17053.

(17) Chen, Z.; Cotterell, B.; Wang, W. The fracture of brittle thin films on compliant substrates in flexible displays. *Eng. Fract. Mech.* **2002**, *69*, 597−603.

(18) Peng, C.; Jia, Z.; Neilson, H.; Li, T.; Lou, J. In Situ Electro-Mechanical Experiments and Mechanics Modeling of Fracture in Indium Tin Oxide-Based Multilayer Electrodes. *Adv. Eng. Mater.* **2013**, *15*, 250−256.

(19) Leterrier, Y.; Medico, L.; Demarco, F.; Månson, J.-A.; Betz, U.; Escola, M.; Kharrazi Olsson, M.; Atamny, F. Mechanical integrity of transparent conductive oxide films for flexible polymer-based displays. *Thin Solid Films* **2004**, *460*, 156−166.

(20) Saleh, M. N.; Lubineau, G. Understanding the mechanisms that change the conductivity of damaged ITO-coated polymeric films: A micro-mechanical investigation. *Sol. Energy Mater. Sol. Cells* **2014**, *130*, 199−207.

(21) Machinaga, H.; Ueda, E.; Mizuike, A.; Takeda, Y.; Shimokita, K.; Miyazaki, T. Effects of annealing temperature on mechanical

durability of indium-tin oxide film on polyethylene terephthalate substrate. *Thin Solid Films* **2014**, *559*, 36−39.

(22) Guo, P.; Schaller, R. D.; Ocola, L. E.; Ketterson, J. B.; Chang, R. P. Gigahertz Acoustic Vibrations of Elastically Anisotropic Indium−Tin-Oxide Nanorod Arrays. *Nano Lett.* **2016**, *16*, 5639−5646.

(23) Veith, M.; Bubel, C.; Grobelsek, I. Investigation of morphological and electrical characteristics of tin doped indium oxide layers produced by a quasi single source precursor system. *Thin Solid Films* **2012**, *524*, 67−74.

(24) Bhopal, M. F.; Lee, D. W.; Rehman, A.-u.; Lee, S. H. Influence of annealing temperature on structural properties of ITO thin-films on graphite substrate. *Vacuum* **2016**, *133*, 108−113.

(25) Sahu, B. B.; Wen, L.; Kim, S. H.; Han, J. G. Study of plasma characteristic and properties of flexible ultra-thin ITO films prepared by large area 3-D confined and planar magnetron sputtering. *Vacuum* **2019**, *165*, 246−253.

(26) Fang, X.; Mak, C.; Zhang, S.; Wang, Z.; Yuan, W.; Ye, H. Pulsed laser deposited indium tin oxides as alternatives to noble metals in the near-infrared region. *J. Phys.: Condens. Matter* **2016**, *28*, 224009.

(27) Lacroix, B.; Santos, A.; Hurand, S.; Corvisier, A.; Paumier, F.; Girardeau, T.; Maudet, F.; Dupeyrat, C.; García, R.; Morales, F. Nanostructure and physical properties control of indium tin oxide films prepared at room temperature through ion beam sputtering deposition at oblique angles. *J. Phys. Chem. C* **2019**, *123*, 14036−14046.

(28) Zhinong, Y.; Yuqiong, L.; Fan, X.; Zhiwei, Z.; Wei, X. Properties of indium tin oxide films deposited on unheated polymer substrates by ion beam assisted deposition. *Thin Solid Films* **2009**, *517*, 5395−5398.

(29) Chommaux, T.; Godard, P.; Thiaudière, D.; Renault, P. Impact of the brittle layers on the electrical and mechanical behaviours of 18 nm Ag layers in indium tin oxide-silver stackings. *Thin Solid Films* **2025**, *826*, 140765.

(30) Chommaux, T.; Renault, P.; Thiaudière, D.; Godard, P.; Paumier, F.; Girardeau, T.; Hurand, S.; Goudeau, P. In situ electrical and mechanical study of Indium Tin Oxide films deposited on polyimide substrate by Xe ion beam sputtering. *Thin Solid Films* **2022**, *741*, 139035.

(31) Marezio, M. Refinement of the crystal structure of In_2O_3 at two wavelengths. *Acta Crystallogr.* **1966**, *20*, 723−728.

(32) Geandier, G.; Thiaudière, D.; Randriamazaoro, R. N.; Chiron, R.; Djaziri, S.; Lamongie, B.; Diot, Y.; Le Bourhis, E.; Renault, P.-O.; Goudeau, P.; et al. Development of a synchrotron biaxial tensile device for in situ characterization of thin films mechanical response. *Rev. Sci. Instrum.* **2010**, *81*, 103903.

(33) Djaziri, S.; Renault, P.-O.; Hild, F.; Le Bourhis, E.; Goudeau, P.; Thiaudière, D.; Faurie, D. Combined synchrotron X-ray and image-correlation analyses of biaxially deformed W/Cu nano-composite thin films on Kapton. *J. Appl. Crystallogr.* **2011**, *44*, 1071−1079.

(34) Van der Pauw, L. J. A method of measuring specific resistivity and Hall effect of discs of arbitrary shape. *Philips Res. Rep.* **1958**, *13*, 1−9.

(35) Zardetto, V.; Brown, T. M.; Reale, A.; Di Carlo, A. Substrates for flexible electronics: A practical investigation on the electrical, film flexibility, optical, temperature, and solvent resistance properties. *J. Polym. Sci., Part B: Polym. Phys.* **2011**, *49*, 638−648.

(36) Gheidari, A. M.; Behafarid, F.; Kavei, G.; Kazemzad, M. Effect of sputtering pressure and annealing temperature on the properties of indium tin oxide thin films. *Mater. Sci. Eng. B* **2007**, *136*, 37−40.

(37) Kulkarni, A. K.; Schulz, K.; Lim, T.-S.; Khan, M. Electrical, optical and structural characteristics of indium-tin-oxide thin films deposited on glass and polymer substrates. *Thin Solid Films* **1997**, *308*, 1−7.

(38) Legeay, G. Couches minces amorphes d'ITO: Caractérisation, structure, évolution et fonctionnalisation sous rayonnements UV. Ph.D. Thesis, Université Rennes, 2011; Vol. *1*.

(39) Holzwarth, U.; Gibson, N. The Scherrer equation versus the 'Debye-Scherrer equation. *Nat. Nanotechnol.* **2011**, *6*, 534.

(40) Kim, J.-H.; Lee, J.-H.; Heo, Y.-W.; Kim, J.-J.; Park, J.-O. Effects of oxygen partial pressure on the preferential orientation and surface morphology of ITO films grown by RF magnetron sputtering. *J. Electroceram.* **2009**, *23*, 169−174.

(41) Park, J.-W.; Kim, G.; Lee, S.-H.; Kim, E.-H.; Lee, G.-H. The effect of film microstructures on cracking of transparent conductive oxide (TCO) coatings on polymer substrates. *Surf. Coat. Technol.* **2010**, *205*, 915−921.

(42) Thompson, C. V.; Carel, R. Stress and grain growth in thin films. *J. Mech. Phys. Solids* **1996**, *44*, 657−673.

(43) Hauk, V. *Structural and Residual Stress Analysis by Non-destructive Methods: Evaluation-Application-Assessment*; Elsevier, 1997.

(44) Klimashin, F. F.; Učík, M.; Matas, M.; Holec, D.; Beutner, M.; Hackert-Oschätzchen, M.; Xomalis, A.; Schwiedrzik, J. J.; Klusoň, J.; Jílek, M.; Lümkemann, A.; Michler, J.; et al. Nitrogen's whereabouts and role in structure-property relationships. *Acta Mater.* **2025**, *294*, 121158.

(45) Debelle, A.; Abadias, G.; Michel, A.; Jaouen, C. Stress field in sputtered thin films: Ion irradiation as a tool to induce relaxation and investigate the origin of growth stress. *Appl. Phys. Lett.* **2004**, *84*, 5034−5036.

(46) Withers, P.; Preuss, M.; Steuwer, A.; Pang, J. Methods for obtaining the strain-free lattice parameter when using diffraction to determine residual stress. *Appl. Crystallogr.* **2007**, *40*, 891−904.

(47) Rafaja, D.; Wüstefeld, C.; Baehtz, C.; Klemm, V.; Dopita, M.; Motylenko, M.; Michotte, C.; Kathrein, M. Effect of internal interfaces on hardness and thermal stability of nanocrystalline $Ti_{0.5}Al_{0.5}N$ coatings. *Metall. Mater. Trans. A* **2011**, *42*, 559−569.

(48) Lacroix, B.; Paumier, F.; Gaboriaud, R. J. Crystal defects and related stress in Y_2O_3 thin films: origin, modeling, and consequence on the stability of the C-type structure. *Phys. Rev. B: Condens. Matter Mater. Phys.* **2011**, *84*, 014104.

(49) Edwards, P. P.; Sienko, M. J. Universality aspects of the metal-nonmetal transition in condensed media. *Phys. Rev. B* **1978**, *17*, 2575.

(50) Fan, J. C.; Goodenough, J. B. X-ray photoemission spectroscopy studies of Sn-doped indium-oxide films. *J. Appl. Phys.* **1977**, *48*, 3524−3531.

(51) Jung, Y. S. A spectroscopic ellipsometry study on the variation of the optical constants of tin-doped indium oxide thin films during crystallization. *Solid State Commun.* **2004**, *129*, 491−495.

(52) Bel Hadj Tahar, R.; Ban, T.; Ohya, Y.; Takahashi, Y. Optical, structural, and electrical properties of indium oxide thin films prepared by the sol-gel method. *J. Appl. Phys.* **1997**, *82*, 865−870.

(53) Chung, C.-H.; Song, T.-B.; Bob, B.; Zhu, R.; Yang, Y. Solution-processed flexible transparent conductors composed of silver nanowire networks embedded in indium tin oxide nanoparticle matrices. *Nano Res.* **2012**, *5*, 805−814.

(54) Txintxurreta, J.; G-Berasategui, E.; Ortiz, R.; Hernandez, O.; Mendizábal, L.; Barriga, J. Indium tin oxide thin film deposition by magnetron sputtering at room temperature for the manufacturing of efficient transparent heaters. *Coatings* **2021**, *11*, 92.

(55) Renault, P.; Sadat, T.; Godard, P.; He, W.; Guerin, P.; Géandier, G.; Blanc, N.; Boudet, N.; Goudeau, P. Continuous cyclic deformations of a Ni/W film studied by synchrotron X-ray diffraction. *Surf. Coat. Technol.* **2017**, *332*, 351−357.

(56) Povedano, A. T.; Michel, A.; Haltz, E.; Godard, P.; Thiaudière, D.; Mocuta, C.; Joly, P.; Mahmoud, H. B.; Girodon-Boulandet, N.; Zighem, F.; et al. Influence of applied deformation on magnetic properties of ferromagnetic Ni60Fe40 thin films deposited on polymeric substrate. *Surf. Coat. Technol.* **2025**, *517*, 132795.

(57) d'Heurle, F.; Harper, J. Note on the origin of intrinsic stresses in films deposited via evaporation and sputtering. *Thin Solid Films* **1989**, *171*, 81−92.

(58) Putz, B.; Edwards, T. E.; Huszar, E.; Gruber, P. A.; Gradwohl, K.-P.; Kreiml, P.; Többens, D. M.; Michler, J. Electromechanical behavior of Al/Al_2O_3 multilayers on flexible substrates: insights from

in situ film stress and resistance measurements. *Adv. Eng. Mater.* **2023**, *25*, 2200951.
(59) Faurie, D.; Renault, P.-O.; Le Bourhis, E.; Goudeau, P. Study of texture effect on elastic properties of Au thin films by X-ray diffraction and in situ tensile testing. *Acta Mater.* **2006**, *54*, 4503−4513.
(60) Cleveland, W. S. Robust locally weighted regression and smoothing scatterplots. *J. Am. Stat. Assoc.* **1979**, *74*, 829−836.
(61) Djaziri, S.; Renault, P.-O.; Le Bourhis, E.; Goudeau, P.; Faurie, D.; Geandier, G.; Mocuta, C.; Thiaudière, D. Comparative study of the mechanical properties of nanostructured thin films on stretchable substrates. *J. Appl. Phys.* **2014**, *116*, 093504.
(62) Oh, S. J.; Kwon, J. H.; Lee, S.; Choi, K. C.; Kim, T.-S. Unveiling the Annealing-Dependent Mechanical Properties of Freestanding Indium Tin Oxide Thin Films. *ACS Appl. Mater. Interfaces* **2021**, *13*, 16650−16659.

https://doi.org/10.1021/acsami.5c21501
ACS Appl. Mater. Interfaces 2026, 18, 23364−23375